High temperature superconductor Na_2B_2H stabilized by hydrogen intercalation under ambient pressure.

Wendi Zhao[1], Defang Duan[1]*, Zhengtao Liu[1], Zihao Huo[1], Shumin Guo[1], Decheng An[1] and Tian Cui*[1,2], Maosheng Miao[3,4,]

[1]*State Key Laboratory of Superhard Materials, College of Physics, Jilin University, Changchun 130012, China*

[2]*Institute of High Pressure Physics, School of Physical Science and Technology, Ningbo University, Ningbo 315211, China*

[3]*Department of Chemistry and Biochemistry, California State University, Northridge, California 91220, USA*

[4]*Department of Earth Science, University of California Santa Barbara, California 93106, USA*

Abstract

Hydrogenated low-dimensional materials have attracted much attention due to their potential high-temperature superconductivity. Here, we propose a new strategy for hydrogen intercalation tuning the stability and superconductivity of the boron honeycomb sublattice, and predict an unprecedented layered compound Na_2B_2H, which hosts excellent superconductivity. Strikingly, the superconducting transition temperature (T_c) of Na_2B_2H is as high as 42 K at ambient pressure. The T_c value can be further increased to 63 K under 5 % biaxial tensile strain. The excellent superconductivity originates from the strong electron-phonon coupling between the σ-bonding bands near the Fermi level and the B-B stretching optical E' modes. The chemical template produced by the hydrogen-embedded Na ion layer stabilizes the boron honeycomb sublattice well. Furthermore, the introduction of ionic hydrogen adjusts the Fermi level and the coupling vibration with Na ions effectively maintains the dynamic stability of the structure. Na_2B_2H represents a new family of hydrogen-intercalated high-temperature superconductors, and this tuning strategy can be further extended to more layered compounds.

Introduction

Since the discovery of superconductivity, the exploration of superconductors hosting high-temperature and even room-temperature superconductivity has been an important research goal of the scientific community. The discovery of the superconducting transition temperature of ~ 39 K in MgB_2 has reignited interest in conventional superconductors[1], whose excellent superconductivity originates from the strong coupling between the σ-states and bond-stretching boron phonons[2-5]. Subsequently, a series of MgB_2-type layered compounds have been extensively studied, usually involving chemical doping[6-8], applying strain[9, 10], hydrogenation[9, 11] and other strategies to further optimize superconductivity. For example, C doping further enhances the electron-phonon coupling between σ bands and bond-stretching optical phonon modes in MgB_3C_3, with a maximum T_c value of 59 K[12]. $Mg_2B_4C_2$, a MgB_2-like two-dimensional (2D) material with charge neutral inert surfaces, hosts T_c values up to 48 K [13]. Previous studies have shown that graphite-like layered materials intercalated with alkali or alkaline earth metals usually exhibit enhanced superconductivity[14-18]. The LiB_2C_2 hosted a high T_c value of 92 K due to the strongly coupling of the σ electrons with the E_u and E_g phonon modes, and the T_c value was further increased to 125 K by applying biaxial tensile strain[17]. Furthermore, the predicted T_c values of Li_2B_3C and $Li_4B_5C_3$ are 36.8 K and 16.8 K, respectively [18].

According to Bardeen-Cooper-Schrieffer (BCS) theory[19], light elements are promising to induce strong coupling phonon-mediated superconductivity. In particular, in recent years, a series of superconducting hydrogen-rich materials have been predicted to host remarkable high-temperature and even room-temperature superconductivity (e.g. H_3S (203 K at 155 GPa) [20-22], LaH_{10} (250-260 K at 180 GPa)[23-27], CaH_6 (215 K at 172 GPa)[28-30]), however, the extremely high stable pressure of such materials limits their practical application. Therefore, one of the most critical challenges is to develop a new class of superconductors that can host high-temperature superconductivity at ambient pressure. Interestingly, many hydrogen-functionalized 2D materials exhibit enhanced superconductivity, relying on the intrinsic advantage of hydrogen-driven strong electron-phonon coupling. For example, the hydrogenated monolayer MgB_2 (H-MgB_2) is predicted to host a T_c value of 67 K, which can be increased to 100 K by biaxial tensile strain[9]. The hydrogenated MXene material Mo_2NH_2 hosted a T_c value of 32 K[31], much higher than the pristine Mo_2N[32]. In particular, hydrogenation induces significant superconductivity in some 2D materials

whose parent structure is not superconducting, such as 2H-$Mo_2C_3H_2$[33] and $Ti_2B_2H_4$[11] hosts T_c of 53 K and 48.6 K, respectively. These materials expand the research scope of 2D superconducting materials, especially their stability under ambient pressure is conducive to practical applications, such as the potential application prospects in the construction of nano-superconducting devices[34].

In this letter, we propose a new strategy that relies on the chemical template generated by the hydrogen-intercalated metal ion layer to stabilize the boron honeycomb sublattice, thereby hosting excellent superconductivity. We reported an unprecedented Na_2B_2H that stabilizes to ambient pressure, hosting T_c value up to ~ 42 K. The excellent superconductivity is attributed to the strong coupling between the σ-bonding bands and the in-plane phonon vibration modes of the honeycomb B layers, especially the intralayer bond-stretching E' modes. The chemical template generated by the hydrogen-embedded Na ion layer stabilizes the honeycomb B layer well and induces high electron density of states at the Fermi level. In particular, the application of appropriate biaxial tensile strain leads to the softening of the B-related E' modes, which enhances the electron-phonon coupling, and the highest T_c value can reach 63 K. These findings provide new insights into understanding the superconductivity and stability of hydrogen-intercalated metal borides, and promising to expand to more layered compounds.

Computational details

All calculations of structural optimization and electronic properties are performed within the framework of density functional theory (DFT), as implemented in Vienna ab initio simulation package (VASP) code[35]. The ion-electron interactions part was implemented with the projector augmented wave method[36, 37], where $1s^1$, $2s^22p^1$, $2s^22p^63s^1$ are considered as valence electrons for H, B, Na atoms, respectively. The Perdew-Burke-Ernzerhof parametrization within the generalized gradient approximation was performed to describe the exchange-correction function[38]. The cut-off energy was set to 1000 eV, and the Monkhorst-Pack k-mesh with grid spacing of $2\pi\times0.02$ Å^{-1} was adopted. The phonon spectra and electron-phonon coupling (EPC) calculations were carried out using the Quantum ESPRESSO code[39]. Ultra-soft pseudopotentials and a kinetic energy cut-off of 80 Ry were adopted. The Brillouin zone (BZ) k-point grid of $24\times24\times16$ and q-point mesh of $6\times6\times4$ were used to accurately calculate the electron-phonon coupling. The mode-resolved EPC constant λ_{qv} is defined as

$$\lambda_{\boldsymbol{qv}} = \frac{\gamma_{\boldsymbol{qv}}}{\pi\hbar N(E_F)\omega_{\boldsymbol{qv}}^2} \quad (1)$$

Where $\omega_{\boldsymbol{qv}}$ is the phonon frequency of the vth phonon mode with wave vector $\boldsymbol{q}$, and $N(E_F)$ is the DOS at the Fermi level. The phonon linewidth $\gamma_{\boldsymbol{qv}}$ can be estimated by

$$\gamma_{\boldsymbol{qv}} = \frac{2\pi\omega_{\boldsymbol{qv}}}{\Omega_{BZ}} \sum_{k,n,m} \left| g^{v}_{kn,k+qm} \right|^2 \delta(\epsilon_{\boldsymbol{kn}} - \epsilon_F) - \delta\left(\epsilon_{\boldsymbol{k+qm}} - \epsilon_F\right) \quad (2)$$

where Ω_{BZ} is the volume of the Brillouin zone (BZ), $\epsilon_{\boldsymbol{kn}}(\epsilon_{\boldsymbol{k+qm}})$ indicate the Kohn-Sham energy, and $g^{v}_{kn,k+qm}$ represents the EPC matrix elements.

The Eliashberg spectral function $\alpha^2F(\omega)$ is then calculated by[40-42],

$$\alpha^2F(\omega) = \frac{1}{2\pi N(E_F)} \sum_{\boldsymbol{qv}} \delta\left(\omega - \omega_{\boldsymbol{qv}}\right) \frac{\gamma_{\boldsymbol{qv}}}{\omega_{\boldsymbol{qv}}} \quad (3)$$

$$\lambda = 2\int_0^{\infty} \frac{\alpha^2\mathrm{F}(\omega)}{\omega} d\omega = \sum_{\boldsymbol{qv}} \lambda_{\boldsymbol{qv}} \quad (4)$$

T_c is estimated by the full Allen-Dynes formula [40],

$$T_c = \frac{f_1 f_2 \omega_{log}}{1.2} \exp\left[-\frac{1.04(1+\lambda)}{\lambda - \mu^*(1+0.62\lambda)}\right] \quad (5)$$

where μ^* is the coulomb pseudopotential parameter and is set to a typical value of 0.1-0.13. f_1 and f_2 are the strong-coupling correction factor and the shape correction factor, respectively. ω_{log} was the logarithmic average of the phonon frequencies,[40]

$$\omega_{log} = \exp\left[\frac{2}{\lambda}\int \frac{d\omega}{\omega} \alpha^2F(\omega) \ln\omega\right] \quad (6)$$

Results and discussion

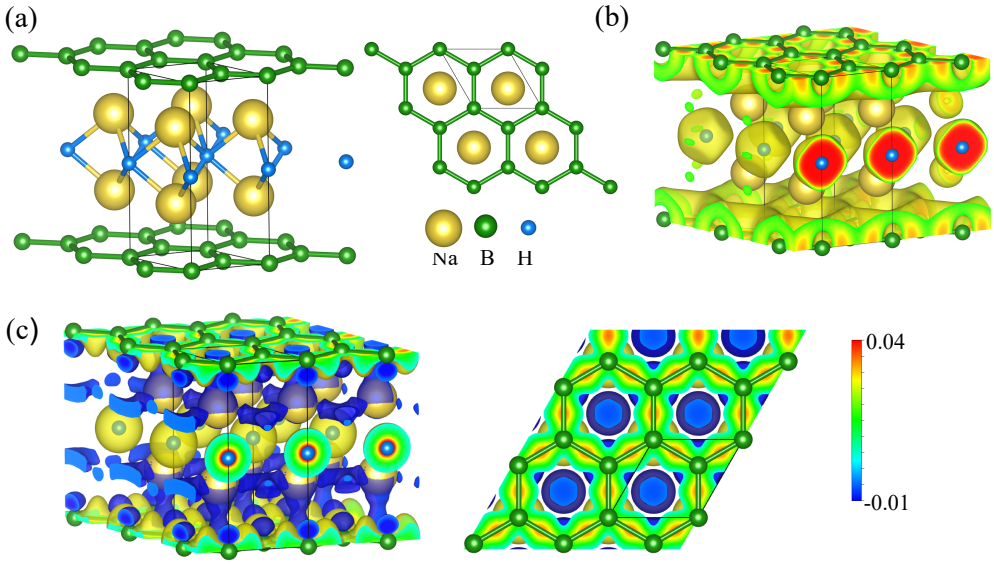

Fig. 1 The structure and electronic properties of Na_2B_2H at 1atm. (a) Solid and top views of Na_2B_2H, (b) Electron localization function (ELF). Isosurface is set to 0.5. (c) The differential charge density. Blue and yellow represent charge loss and accumulation, respectively.

Optimized crystal structure of Na_2B_2H crystallizes in the space group *P*-6*m*2 with lattice constants of a=b=3.07 Å and c = 7.27 Å. The bulk Na_2B_2H consists of a graphene-structure B layer and an atomic H layer, separated by interstitial Na layers (see Figure 1a). The Na atoms are located at the 2i (0.667,0.333,0.293) Wyckoff position, corresponding to the honeycomb center of the B layer. The B atom occupies the 1a (0.000, 0.000,0.000) and 1c (0.333, 0.667,0.000) positions and the H atom occupies the 1b (0.000, 0.000,0.500) position. The vertical distances from the Na atomic layer to the H and B layers are 1.48 Å and 2.16 Å, respectively. In the honeycomb boron layer, the hybridization of atomic orbitals generates sp^2 hybridized σ bond and p_z overlapped π bond, respectively. The B-B bond length is 1.77 Å, and the high electron localization appears near the bond center, confirming the B-B strong covalent bond. There is almost no electron localization between Na-B and Na-H, revealing the formation of ionic bonds (see Figure 1b). Na atoms with low electronegativity donate abundant electrons to H and B atoms. Bader charge analysis shows that the Na atom transfers electrons 0.78 |e| and 0.79 |e| to H atom and B layer, respectively. The differential charge density can clearly show the charge transfer between atoms. Here, we define

$$\Delta\rho = \rho_{Na_2B_2H} - \rho_{Na} - \rho_B - \rho_H$$

The $\rho_{Na_2B_2H}$ and ρ_{Na}, ρ_B and ρ_H here represent the charge densities of bulk Na_2B_2H and

isolated Na, B and H atoms, respectively. As shown in the Figure1c, the blue region of the encapsulated Na indicates charge deficit, while the yellow region around the H and B atoms indicates charge accumulation. Note that the significant charge accumulation in the middle of the B-B bond effectively maintains the stability of the honeycomb B layer.

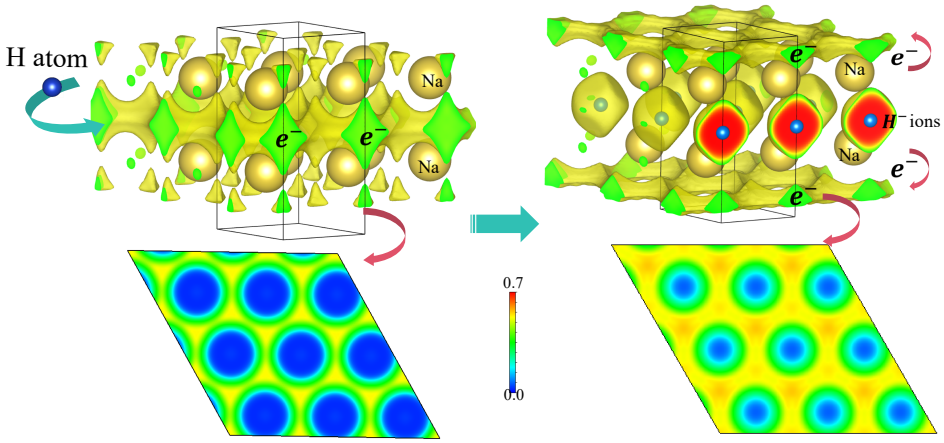

Fig.2 Electron localization functions (above) of isolated Na and Na_2H lattices, which are directly stripped from Na_2B_2H. Isosurface is set to 0.5. The cross section of the electron localization outside the Na ion layer (below).

In order to further understand the effect of hydrogen intercalation on the stability of Na_2B_2H, we consider the chemical template effect[43], which well reveals the stability of superconducting hydrides. Specifically, electron localization in the interstitial region of the metal sublattice assists in the formation and stabilization of the hydrogen covalent network. In this work, we calculated the ELFs of isolated Na lattice and Na_2H lattice. Figure 2 illustrates the effect of H atom intercalation on the electron localization in the interstitial region of Na lattice. The interstitial electrons of the isolated Na lattice accumulate mainly between the Na ionic layers. Differently, H atoms embedded in the Na ionic layer capture part of the interstitial electrons and other extra electrons are driven away from the Na ionic layer due to the Coulomb repulsion of H^- ions. Therefore, the outer side of the Na_2H ion layer shows more significant electron localization than the isolated Na ion layer, and these interstitial anionic electrons (IAEs) have a significant contribution near the Fermi level. Interestingly, these extra electrons are not only close to the boron layer, but also show a honeycomb distribution that matches well with the boron sublattice, and thus are more easily captured by the B layer enhancing its stability (see Figure S2-4). Furthermore, the Crystal Orbital Hamilton Population (COHP) analysis can quantify the interatomic bonding strength [44, 45]. The calculated ICOHP

value of the B-B bond reaches -6.28 (see Figure S5), similar to MgB_2[46]. The smaller ICOHP values of Na-B and Na-H further confirms the formation of ionic bonds. In particular, the B-B covalent bond strength (|ICOHP|=6.28) in Na_2B_2H is higher than that (|ICOHP|=5.71) in Na_2B_2. Therefore, the chemical template generated by Na_2H is more conducive to the stability of the B layer than the isolated Na lattice. In addition, compared with *P*6/*mmm* Na_2B_2, the crystalline point group symmetry information further reveals that Na and H atoms hosted in *P*-6*m*2 Na_2B_2H are easier to couple with B atoms (see Table S1-2). These results provide an important reference for understanding the stability of the hydrogen intercalation metal borides.

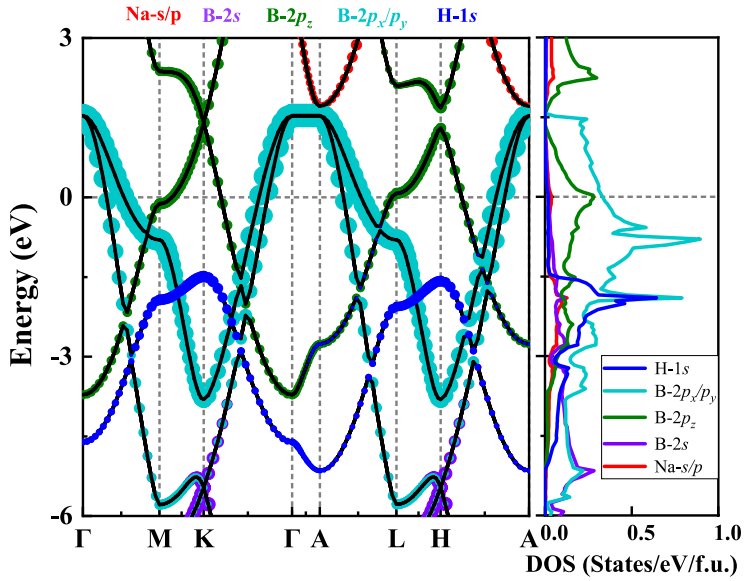

Fig. 3 Calculated energy band structures with orbital projections and orbital-resolved density of states (DOS) of Na_2B_2H at 1 atm.

The calculated band structure and projected density of states (PDOS) clearly reveal the intrinsic metallicity of Na_2B_2H (see Figure3). Several steep electron pockets appear near the Fermi level, and the nearly parallel bands along the Γ-A direction reflect the layered characteristics of the system. The simultaneous occurrence of flat and steep bands near the Fermi level has been suggested as favorable conditions for enhancing electron pairing, which is essential to superconducting behavior. The orbital-resolved band structure highlights that the two bands crossing the Fermi level are mainly derived from the B-2$p_{x/y}$ orbital (σ band) and the B-2p_z orbital (π band), which play an important role in metallicity. The Van Hove singularity of the B-2p_z orbit appears at the Fermi level, which is caused by the weak dispersion bands near the M and L points. The contribution of Na and H atoms to the DOS at the Fermi energy level is weak, which is significantly different from that of

hydrogenated monolayer MgB_2, whose π-H*s* states formed by hybridization of B-p_z and H-*s* orbitals dominate the electronic states at the Fermi level[9]. However, the role of H atom in the band structure can be elucidated by comparison with Na_2B_2. Compared with the band structure of Na_2B_2, the introduction of H atoms lowers the Fermi energy (see Figure S6), which is the key for the B-2p_z orbital to show the Van Hove peak at the Fermi level. At the same time, the ion interaction of Na-H contributes to the interlayer binding and stabilize the structure.

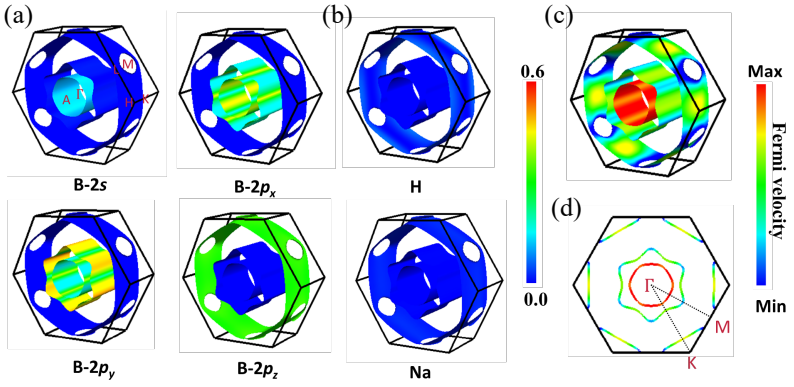

Fig.4 (a-b) Calculated atomic orbital-resolved Fermi sheets for Na_2B_2H. (c) The Fermi surface of each band colored by the value of the Fermi velocity. Red color indicates high velocity; blue color denotes low velocity. (d) The cross section of Fermi surface in Brillouin zone.

Figure 4 shows the orbital-resolved Fermi surface. The Fermi surface of Na_2B_2H consists of two bands. The first band is cylindrical Fermi surface centered at Γ point, originating mainly from B-*s* and B-p_x/p_y orbitals. The second band consists of a petal-shaped Fermi sheet (dominated by B-p_x/p_y) surrounding the Γ point and a hexagonal Fermi sheet (mainly from B-2p_z) near the boundary of the Brillouin zone. The electronic states of Na and H only have a weak contribution to the Fermi sheet around the Brillouin zone boundary. Therefore, the orbital-resolved Fermi surface is well consistent with the band structure. Taking the K-Γ direction as an example, the electronic bands pass through the Fermi level three times, and the formed electron pocket comes from the B-p_x/p_y and B-p_z states, while the degenerate hole pockets at the Γ point mainly comes from the B-p_x/p_y. Furthermore, the Fermi velocity v_F reflects the different slopes of the bands that constitute the Fermi surface, especially related to the potential Fermi surface nesting. The high Fermi velocity appears in the adjacent concentric cylindrical and petal-shaped Fermi sheets. Note that strong interband pairing interactions contribute to enhanced electron-phonon coupling and hence superconductivity. In order to further investigate the potential Fermi surface nesting, we calculate

the nesting function ξ(Q) of Na_2B_2H along the specified high-symmetric path (Γ-M-K-H-A-L) in the Brillouin zone. The nesting function ξ(Q) is defined as follows[47],

$$\xi(\boldsymbol{Q}) = \frac{1}{N}\sum_{\boldsymbol{k},i,j} \delta(\varepsilon_{\boldsymbol{k},i} - \varepsilon_F)\delta(\varepsilon_{\boldsymbol{k}+\boldsymbol{Q},j} - \varepsilon_F)$$

The N represents the number of k points, $\varepsilon_{\boldsymbol{k},i}$ is the Kohn-Sham eigenvalues, ε_F is the Fermi energy and i, j are the indices of energy bands. The calculation employs 9216 k points and 2783232 $k + Q$ points to attain their respective energy eigenvalues. The high nested function ξ(Q) will highlight the possibility of Fermi surface nesting. The highest nested function value at Γ reflects the nesting of the Fermi surface itself, which is expected (see Figure5). Strikingly, the sharp peak of ξ (Q) appears at point A, reflecting strong Fermi surface nesting, which is also shown in previously reported layered materials[48, 49]. Strong electron-phonon coupling induced by nested electronic states will significantly enhance the superconductivity.

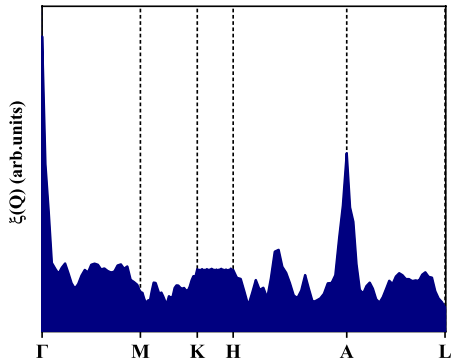

Fig.5 The calculated nesting function ξ (Q) of Na_2B_2H along some special Q trajectories.

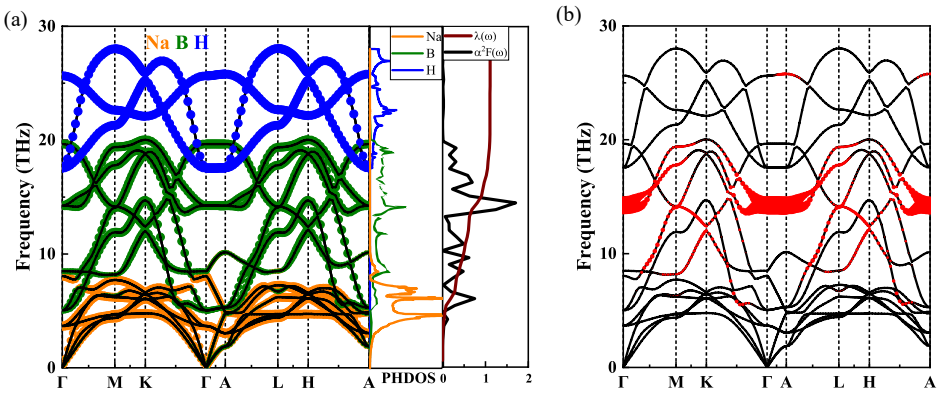

Fig.6 (a) The atom-resolved phonon dispersion curves, projected phonon density of states (PHDOS), and Eliashberg spectral function $\alpha^2F(\omega)$ together with the electron–phonon integral $\lambda(\omega)$ for Na_2B_2H at 1 atm. (b) The phonon spectra with red dots indicating phonon linewidths for Na_2B_2H at 1atm. (c) The phonon spectra of Na_2B_2 at 1atm.

The phonon dispersion curve, projected phonon density of states (PHDOS), Eliashberg spectral

function $\alpha^2F(\omega)$ together with the electron-phonon integral $\lambda(\omega)$ of Na_2B_2H were illustrated in Fig. 6. The absence of any imaginary frequencies along the high-symmetry lines of the Brillouin zone confirms the dynamic stability. All of these optical modes are found to be quite dispersive, with the exception of those along the Γ-A direction, which is related to the layered structure of Na_2B_2H. The dispersive modes in the low-frequency range (<10 THz) are mainly related to the local vibrations of Na atoms. Six low-frequency optical modes are present at the zone center Γ, two of which are degenerate modes with frequencies of 122 cm^{-1} and 170 cm^{-1}, respectively. The vibration modes in the mid-frequency (10-20 THz) region are dominated by B atoms. In particular, the double degenerate mode at ~ 14.20 THz (473.57 cm^{-1}) significantly contributes to the EPC, which involves the degenerate in-plane bond-stretching E' modes along Γ-A, similar to the E_{2g} modes of MgB_2[50]. The high-frequency (> 20 THz) optical branches are mainly characterized by the vibration modes of the H atoms. Although these modes have only a weak contribution to EPC, the hydrogen atom is easily coupled to the vibration of other atoms due to its minimal mass, which effectively maintains the dynamic stability of Na_2B_2H. This is different from the imaginary frequency of Na_2B_2 at Γ point (see Figure S6). Furthermore, the red dots decorating the phonon spectrum represent phonon linewidth, the size of which reflects the contribution to the electron-phonon coupling. Obviously, the two doubly degenerate E' modes associated with the B-B in-plane stretching vibration near the Γ and A points dominate the maximum phonon linewidth. Hence, the strong coupling between in-plane vibrations and σ bands significantly increases the total EPC. As a result, the intense peak of the Eliashberg spectral function appears at about 15 THz, corresponding to the rapid rise of $\lambda(\omega)$. The vibration modes in the intermediate frequency region dominated by B contribute up to 52 % to the total EPC. The calculated λ and ω_{log} of Na_2B_2H at 1 atm are 1.11 and 488.5, respectively. Further the T_c value estimated by A-D equation is as high as 42 K, which is higher than that of MgB_2.

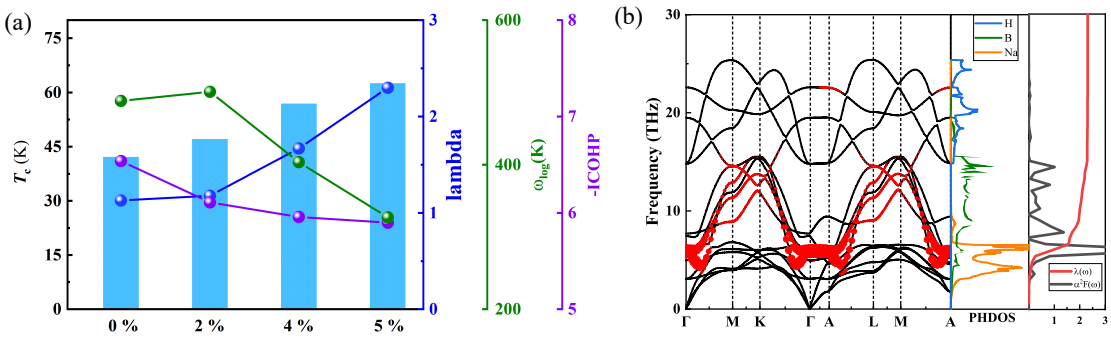

Fig. 7 (a) The T_c values and related parameters of Na_2B_2H under different biaxial tensile strains. (b) Phonon dispersion curves, PHDOS, and $\alpha^2F(\omega)$ together with $\lambda(\omega)$ of Na_2B_2H at 1 atm and 5 % tensile strain. The phonon spectra with red dots indicating phonon linewidths.

We investigate the effect of different biaxial tensile strains on phonon dispersion. Na_2B_2H is still dynamically stable under the tensile strain range of 0 -5 %. The tensile strain effect leads to the softening of phonon modes, especially in the E' modes in the intermediate frequency region, which is attributed to the weakening of the strength of B-B covalent bonds (see Figure 7). Notably, the significant softening of the phonon modes effectively enhances the electron-phonon coupling. The E' modes decrease to 5 THz at 5 % tensile strain, and the corresponding spectral function peak moves to the low frequency region. Although ω_{log} decreases with the increase of strain, the increase of λ significantly contributes to the T_c value. The calculated T_c value at 5 % tensile strain is 63 K, which is close to the liquid nitrogen temperature.

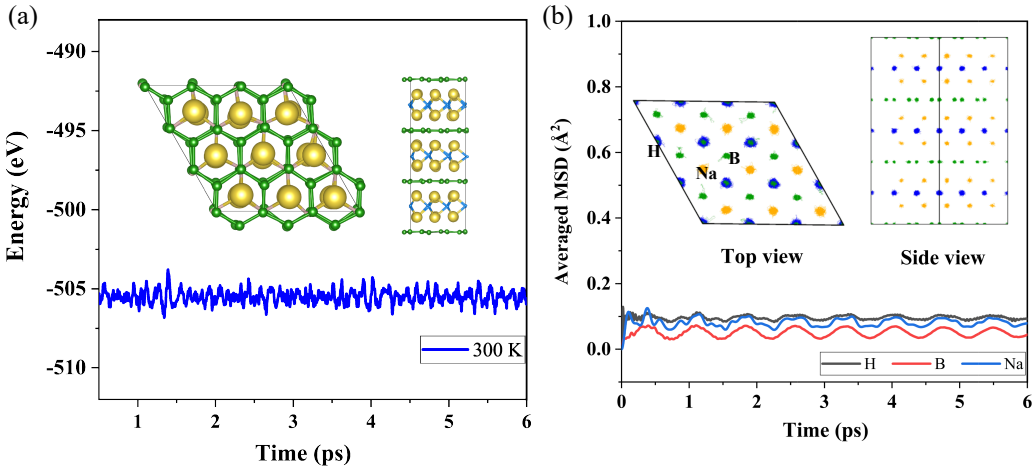

Fig. 8 (a) Energies as a function of AIMD simulation time at 300 K and 1atm. The insets are structural snapshot of Na_2B_2H at 6 ps, respectively. (b) The mean square displacement curve of Na_2B_2H during 6 ps AIMD simulations. The insets are atomic trajectories (H in blue, B in green and Na in yellow).

Cohesive energy is a widely accepted parameter for evaluating the thermally stable of materials and the calculation formula is as follows: $E_{coh} = [2E_{Na} + 2E_B + E_H - E_{Na_2B_2H}]/5$, where E_{Na}, E_B, and E_H are the total energies of the isolated Na, B, and H atoms, respectively; $E_{Na_2B_2H}$ represents the total energy of the Na_2B_2H. The calculated cohesive energy of Na_2B_2H is 3.67 eV/atom, which is higher than that of some materials that have been experimentally synthesized[51, 52]. In order to investigate the thermal stability of Na_2B_2H, we performed ab initio molecular

dynamics (AIMD) simulations under the canonical ensemble (NVT) using the Nosé-Hoover thermostat[53, 54]. The temperature was controlled at 300 K with 3 × 3 × 3 supercells (135 atoms). The running time is 6 ps with 1 fs time step. Figure 8 show the variation of total energies with time during the AIMD steps and the structure snapshots after 6 ps. Na_2B_2H maintained its original configuration well during the AIMD simulations, resulting in total energy fluctuations around a constant temperature value with a small fluctuation range. The mean square displacement (MSD) effectively identifies the pattern of particle movement over time and can well measure the stability of the materials. Figure 8b shows a very small range of fluctuations in the MSD of Na_2B_2H and the atomic trajectories are localized at their respective equilibrium lattice sites. These results confirm the thermodynamic stability of Na_2B_2H and the feasibility of experimental synthesis.

The excellent superconductivity of Na_2B_2H under ambient pressure provides a new platform for the exploration of superconducting materials. Some layered compounds that are isomorphic to Na_2B_2H also host excellent superconductivity, such as K_2B_2H and Na_2C_2H (see Table S3). In particular, NaC_2 is dynamically unstable under ambient pressure, and the predicted T_c value at 100 GPa is 24.7 K[48]. Strikingly, the Na_2C_2H formed by hydrogen intercalation is stable under ambient pressure and the host T_c value is as high as 28 K. We believe that this novel structural prototype will be extended to more layered compounds.

Conclusion

In summary, we propose a strategy for tuning the stability and superconductivity of honeycomb boron layered materials by hydrogen intercalation, which is reflected in the comprehensive investigation of Na_2B_2H. The chemical template produced by the Na ion layer embedded in the H atom stabilizes the boron honeycomb layer well. The predicted T_c value reaches 42 K and further increases to 63 K at 5 % biaxial tensile strain. The excellent superconductivity is mainly due to the strong coupling between the σ electrons and the in-plane stretching of B-B bonds, reflected in the large phonon linewidths and strong Fermi surface nesting. The biaxial tensile strain induces significant softening of B-related E' modes, thus promoting electron-phonon coupling. The introduction of H atoms effectively tunes the electronic structure near the Fermi level, which plays an important role in structural stability and promoting strong electron-phonon coupling. These findings will deepen the understanding of the intrinsic relationship between the structure and

superconductivity of hydrogen-functionalized materials with different structural motifs, and the predicted Na_2B_2H provides a new platform to expand to more superconducting materials under ambient pressure.

Acknowledgements

We thank Professor Maosheng Miao for many interesting and stimulating discussions. This work was supported by the National Natural Science Foundation of China (Grants No. 52072188, No. 12122405, No. 12274169), the National Key Research and Development Program of China (No. 2022YFA1402304), the Program for Science and Technology Innovation Team in Zhejiang (No. 2021R01004), and Jilin Provincial Science and Technology Development Project (No. 20210509038RQ). M.M. acknowledges NSF DMR 1848141, OAC 2117956, the Camille and Henry Dreyfus Foundation, and CSU RSCA grants. Some of the calculations were performed at the High-Performance Computing Center of Jilin University and using TianHe-1(A) at the National Supercomputer Center in Tianjin.

References

[1] Nagamatsu J, Nakagawa N, Muranaka T, et al. Superconductivity at 39 k in magnesium diboride. Nature, 2001, 410(6824): 63-64

[2] Li WX, Li Y, Chen RH, et al. Electron–phonon coupling properties in mgb2 observed by raman scattering. J Phys: Condens Matter 2008, 20(25): 255235

[3] Choi HJ, Roundy D, Sun H, et al. The origin of the anomalous superconducting properties of mgb2. Nature, 2002, 418(6899): 758-760

[4] Kong Y, Dolgov OV, Jepsen O, et al. Electron-phonon interaction in the normal and superconducting states of mathrm mgb2. Phys Rev B, 2001, 64(2): 020501

[5] An JM, Pickett WE. Superconductivity of mathrm mgb2: Covalent bonds driven metallic. Phys Rev Lett, 2001, 86(19): 4366-4369

[6] Liu X, Huang X, Song P, et al. Strong electron-phonon coupling superconductivity in compressed α−mob2 induced by double van hove singularities. Phys Rev B, 2022, 106(6): 064507

[7] Rosner H, Pickett WE, Drechsler SL, et al. Electronic structure and weak electron-phonon coupling intab2. Phys Rev B, 2001, 64(14): 144516

[8] Monni M, Ferdeghini C, Putti M, et al. Role of charge doping and lattice distortions in codoped mg1-x(alli)xb2 compounds Phys Rev B, 2006, 73(21): 214508

[9] Bekaert J, Petrov M, Aperis A, et al. Hydrogen-induced high-temperature superconductivity in two-dimensional materials: The example of hydrogenated monolayer mgb_2. Phys Rev Lett, 2019, 123(7): 077001

[10] Liao XZ, Serquis A, Zhu YT, et al. Strain effect on the critical superconducting temperature of mgb2.

Supercond Sci Technol, 2004, 17(8): 1026-1030
[11] Han Y-L, Li Y-P, Yang L, et al. High-temperature superconductivity in two-dimensional hydrogenated titanium diboride: Ti2b2h4. Mater Today Phys, 2023, 30(100954
[12] Pham T-T, Nguyen D-L. First-principles prediction of superconductivity in mgb3c3. Phys Rev B, 2023, 107(13): 134502
[13] Singh S, Romero AH, Mella JD, et al. High-temperature phonon-mediated superconductivity in monolayer mg2b4c2. npj Quantum Mater, 2022, 7(1): 37
[14] Gauzzi A, Takashima S, Takeshita N, et al. Enhancement of superconductivity and evidence of structural instability in intercalated graphite cac6 under high pressure. Phys Rev Lett, 2007, 98 (6): 067002
[15] Hannay NB, Geballe TH, Matthias BT, et al. Superconductivity in graphitic compounds. Phys Rev Lett, 1965, 14(7): 225-226
[16] Kubozono Y, Eguchi R, Goto H, et al. Recent progress on carbon-based superconductors. Journal of Physics: Condensed Matter, 2016, 28(33): 334001
[17] Gao M, Yan X-W, Lu Z-Y, et al. Strong-coupling superconductivity in mathrm lib2 mathrm c2 trilayer films. Phys Rev B, 2020, 101(9): 094501
[18] Bazhirov T, Sakai Y, Saito S, et al. Electron-phonon coupling and superconductivity in li-intercalated layered borocarbide compounds. Phys Rev B, 2014, 89(4): 045136
[19] Bardeen J, Cooper LN, Schrieffer JR. Microscopic theory of superconductivity. Phys Rev, 1957, 106(1): 162-164
[20] Drozdov AP, Eremets MI, Troyan IA, et al. Conventional superconductivity at 203 kelvin at high pressures in the sulfur hydride system. Nature, 2015, 525(7567): 73-76
[21] Duan DF, Huang XL, Tian FB, et al. Pressure-induced decomposition of solid hydrogen sulfide. Phys Rev B, 2015, 91(18): 180502
[22] Duan D, Liu Y, Tian F, et al. Pressure-induced metallization of dense (h2s)2h2 with high-tc superconductivity. Sci Rep, 2014, 4(1): 6968
[23] Liu HY, Naumov, II, Hoffmann R, et al. Potential high-tc superconducting lanthanum and yttrium hydrides at high pressure. Proc Natl Acad Sci U S A, 2017, 114(27): 6990-6995
[24] Peng F, Sun Y, Pickard CJ, et al. Hydrogen clathrate structures in rare earth hydrides at high pressures: Possible route to room-temperature superconductivity. Phys Rev Lett, 2017, 119(10): 107001
[25] Drozdov AP, Kong PP, Minkov VS, et al. Superconductivity at 250 k in lanthanum hydride under high pressures. Nature, 2019, 569(7757): 528-531
[26] Somayazulu M, Ahart M, Mishra AK, et al. Evidence for superconductivity above 260 k in lanthanum superhydride at megabar pressures. Phys Rev Lett, 2019, 122(2): 027001
[27] Hong F, Yang L, Shan P, et al. Superconductivity of lanthanum superhydride investigated using the standard four-probe configuration under high pressures. Chin Phys Lett, 2020, 37(10): 107401
[28] Ma L, Wang K, Xie Y, et al. High-temperature superconducting phase in clathrate calcium hydride cah6 up to 215 k at a pressure of 172 gpa. Phys Rev Lett, 2022, 128(16): 167001
[29] Wang H, Tse JS, Tanaka K, et al. Superconductive sodalite-like clathrate calcium hydride at high pressures. Proc Natl Acad Sci U S A, 2012, 109(17): 6463-6466
[30] Li Z, He X, Zhang C, et al. Superconductivity above 200 k discovered in superhydrides of calcium. Nat Commun 2022, 13(1): 2863
[31] Bekaert J, Sevik C, Milošević MV. Enhancing superconductivity in mxenes through hydrogenation.

Nanoscale, 2022, 14(27): 9918-9924
[32] Bekaert J, Sevik C, Milošević MV. First-principles exploration of superconductivity in mxenes. Nanoscale, 2020, 12(33): 17354-17361
[33] Jiao N, Liu H-D, Yang L, et al. Hydrogenation-induced high-temperature superconductivity in two-dimensional molybdenum carbide mo2c3. Europhysics Letters, 2022, 138(4): 46002
[34] Paschke F, Birk T, Forti S, et al. Hydrogen-intercalated graphene on sic as platform for hybrid superconductor devices. Adv Quantum Technol, 2020, 3(12): 2000082
[35] Kresse G, Furthmüller J. Efficiency of ab-initio total energy calculations for metals and semiconductors using a plane-wave basis set. Comput Mater Sci, 1996, 6(1): 15-50
[36] Kresse G, Joubert D. From ultrasoft pseudopotentials to the projector augmented-wave method. Phys Rev B 1999, 59(3): 1758-1775
[37] Blöchl PE. Projector augmented-wave method. Phys Rev B 1994, 50(24): 17953-17979
[38] Perdew JP, Burke K, Ernzerhof M. Generalized gradient approximation made simple Phys Rev Lett, 1996, 77(18): 3865-3868
[39] Giannozzi P, Baroni S, Bonini N, et al. Quantum espresso: A modular and open-source software project for quantum simulations of materials. J Phys Condes Matter, 2009, 21(39): 395502
[40] Allen PB, Dynes RC. Transition temperature of strong-coupled superconductors reanalyzed. Phys Rev B, 1975, 12(3): 905-922
[41] McMillan WL. Transition temperature of strong-coupled superconductors. Phys Rev 1968, 167(2): 331-344
[42] Dynes RC. Mcmillan's equation and the tc of superconductors. Solid State Commun, 1972, 10(7): 615-618
[43] Sun Y, Miao M. Chemical templates that assemble the metal superhydrides. Chem, 2023, 9(2): 443-459
[44] Maintz S, Deringer VL, Tchougréeff AL, et al. Lobster: A tool to extract chemical bonding from plane-wave based dft. J Comput Chem, 2016, 37(11): 1030-1035
[45] Deringer VL, Tchougréeff AL, Dronskowski R. Crystal orbital hamilton population (cohp) analysis as projected from plane-wave basis sets. J Phys Chem A, 2011, 115(21): 5461-5466
[46] Zhang S, Feng X, Yang G, et al. The hardness and electrical conduction in tib2 and mgb2: Computational insights. Comput Mater Sci, 2024, 232(112642
[47] Ma Y, Duan D, Shao Z, et al. Divergent synthesis routes and superconductivity of ternary hydride mathrm mgsih6 at high pressure. Phys Rev B, 2017, 96(14): 144518
[48] Yang Q, Zhao K, Liu H, et al. Superconductive sodium carbides with pentagon carbon at high pressures. J Phys Chem Lett, 2021, 12(25): 5850-5856
[49] You J-Y, Gu B, Su G, et al. Emergent kagome electrides. J Am Chem Soc, 2022, 144(12): 5527-5534
[50] Bohnen KP, Heid R, Renker B. Phonon dispersion and electron-phonon coupling in mathrm mgb2 and mathrm alb2. Phys Rev Lett, 2001, 86(25): 5771-5774
[51] Feng B, Fu B, Kasamatsu S, et al. Experimental realization of two-dimensional dirac nodal line fermions in monolayer cu(2)si. Nat Commun 2017, 8(1): 1007
[52] Yang LM, Bacic V, Popov IA, et al. Two-dimensional cu2si monolayer with planar hexacoordinate copper and silicon bonding. J Am Chem Soc, 2015, 137(7): 2757-2762
[53] Nosé S. A unified formulation of the constant temperature molecular dynamics methods. J Chem Phys, 1984, 81(1): 511-519

[54] Hoover WG. Canonical dynamics: Equilibrium phase-space distributions. Phys Rev A, 1985, 31(3): 1695-1697